

MULTIDISCIPLINARY APPROACH FOR THE AERODYNAMIC CHARACTERIZATION OF AN INFLATABLE CLOSED-WING HYBRID HIGH-ALTITUDE PSEUDO-SATELLITE

Eleonora Riccio[1,2], Rocco Bombardieri[1], Alessandro Ceresa[1], Vincenzo Rosario Baraniello[1], Francesco Tufano[1], Giuseppe Persechino[1] & Domenico Coiro[2]

[1]Italian Aerospace Research Center – CIRA, Via Maiorise snc, Capua, 81043, Italy
[2]Department of Industrial Engineering - Aerospace Section, University of Naples Federico II, Via Claudio, Naples, 80125, Italy

Abstract

High-Altitude Pseudo-Satellites (HAPS) represent a cost-effective solution for persistent stratospheric missions; however, hybrid inflatable concepts introduce a strong coupling between internal pressurization, structural deformation, and aerodynamic performance that is often neglected in early-stage design. This work presents a multidisciplinary structural–aerodynamic assessment of a hybrid closed-wing HAPS configuration developed at CIRA within the framework of the *Space It Up* project. Using the explicit solver of LS-DYNA, a nonlinear pressurization analysis is performed on a global finite-element model of the platform, including inflatable spars and outer wing envelope. Two load cases are investigated, corresponding to envelope pressure differentials of 250 Pa and 350 Pa, while maintaining a constant spar pressure differential of 6000 Pa. Subsequently, the nominal CAD geometry and the two selected pressurized configurations are used as input for high-fidelity RANS CFD analyses (using the k–ω SST solver of OpenFOAM) to perform a comparative aerodynamic assessment over a wide range of angles of attack, at asymptotic conditions representative of cruise. With respect to pressurization analyses, results indicate that, compared to the nominal configuration, the inflated equilibrium geometries exhibit modified airfoil shapes, resulting in increased airfoil thickness and local camber modifications. In terms of global wing geometry, the configuration exhibits wingspan reduction, and dihedral variations, particularly near the upper-wing root, and in the vicinity of the joint region, between the upper and lower wings. From an aerodynamic standpoint, these effects result in an upward shift of the lift curve, thereby reducing the cruise angle of attack required to achieve the target C_L at cruise. However, detrimental effects are observed in the drag polar and in the resulting lift-to-drag ratio at the operating point. In addition, the longitudinal pitching moment is significantly affected: the inflated configurations exhibit a persistent nose-down tendency and lacks a natural trim point, thereby implying the need for active control strategies or system-level architectural solutions to achieve trim. Finally, a comparison between the 250 Pa and 350 Pa configurations demonstrates how such aerodynamic characteristics are substantially insensitive to changes in the envelope pressure differential within the observed range. Overall, the results underline how carrying out the aerodynamic design exclusively on the basis of the nominal geometry can lead to non-negligible deviations in performance estimation, and support the inclusion of pressurization-induced shape effects since early-stage design for hybrid inflatable HAPS platforms.

Keywords: Hybrid HAPS; Unconventional aircraft configuration; inflatable structure; Multidisciplinary aircraft design; Aircraft stability and trim

1. Introduction

High-Altitude Pseudo-Satellites (HAPS) have attracted significant interest in recent years as persistent unmanned platforms for Earth observation, surveillance, and telecommunications [1, 2]. Operating in the lower stratosphere, typically between 18 and 20 km, HAPS offer wide-area coverage, low

signal latency, and long endurance, while maintaining substantially lower operational costs compared to space-based systems.

Based on the lift generation mechanism, HAPS architectures are commonly classified as heavier-than-air (HTA) fixed-wing aircraft or lighter-than-air (LTA) buoyant platforms, such as airships [2]. Fixed-wing solutions benefit from aerodynamic efficiency, controllability, and reusability, but are strongly constrained by structural weight and wingspan requirements, especially in low-speed, high-endurance missions. Current industrial benchmarks for such fixed-wing, high-aspect-ratio designs include the AALTO Zephyr, the MIRA Aerospace Apus versions, and the DLR HAP-ALPHA [3], which exemplify the modern state-of-the-art in solar-powered HAPS [4]. Conversely, airships rely primarily on buoyancy to sustain flight, but their scalability toward compact and lightweight platforms is limited by the large volumes required to generate sufficient lift. Modern buoyant platforms like the Sceye airship [5] are being actively deployed to leverage the high-payload capacity and long-station keeping advantages inherent to LTA systems [6]. The multidisciplinary nature of LTA stratospheric airship design, involving strong couplings among aerodynamics, structures, propulsion and energy systems, has already been highlighted in previous studies [7].

Hybrid HAPS concepts, combining aerodynamic and aerostatic lift, represent a promising compromise between these two approaches. By sharing the lift requirement between buoyancy and aerodynamic surfaces, hybrid platforms can reduce structural loads, limit overall dimensions, and improve operational flexibility [8, 9]. Within this context, the Italian Aerospace Research Centre (CIRA) is developing novel hybrid HAPS configurations, including both conventional-wing and closed-wing architectures, conceived to balance aerodynamic efficiency, internal volume availability, and structural feasibility under strict mass and endurance constraints. For this type of platform (i.e., closed-wing configuration), CIRA has patented a specific configuration [WO 2022/167875 A1—PCT/IB2022/050246] tailored to the requirements of Earth observation applications.

Closed-wing configurations trace their theoretical origin to the box-wing lifting system introduced by Prandtl, who demonstrated that, among all possible lifting systems with fixed wingspan and lift, the box-shaped arrangement achieves the minimum induced drag, leading to the concept of the Best Wing System [10]. Prandtl's theoretical findings were later extended toward practical realizations through Munk's stagger theorem [11], which states that, under potential flow assumptions and for a wake aligned with the free stream, the induced drag remains unchanged when lifting surfaces are displaced along the flow direction. Building on these principles, several configurations have been proposed over the years. Early efforts include the Box-Wing conceptual design developed by Lockheed in the 1970s [12], which explored possible applications of Prandtl's lifting system for a transonic mid-range aircraft concept, to the multi-institution effort led by University of Pisa for a 250-seat PrandtlPlane version designed considering aerodynamics, flight mechanics and dynamics, structures, aeroelasticity, engine integration and infrastructures [13]. This activity ultimately led to the H2020-funded PARSIFAL project, aimed at demonstrating how the payload capacity of present aircraft like the Airbus 320 could be raised to the capacity of larger airplanes like A330 by adopting the PrandtlPlane wing system [14].

In the present work, attention is focused on the broader concept of closed-wing layout applied to hybrid HAPS configuration [15]. In addition to the potential for induced-drag reduction, closed-wing layouts offer further advantages that are particularly relevant for hybrid high-altitude, long-endurance platforms. Such arrangement of the lifting surfaces allows additional available internal volume without requiring excessive wingspan growth, thereby facilitating helium capacity and the integration of internal pressurized structural elements. This aspect is especially relevant for inflatable platforms, where the magnitude and distribution of the internal volume directly govern pressurization requirements and, through pressurization-induced shape changes, influence the resulting aerodynamic loads and moments. Such pressure-induced deformations are difficult to capture, as the underlying physics often exceed the capabilities of simplified, static physical models [16].

A previous work conducted at CIRA demonstrated the feasibility of hybrid closed-wing HAPS concepts through preliminary sizing, aerodynamic characterization, and static stability assessment [17]. These studies indicated that, for the considered HAPS application, closed-wing configurations (Fig. 1) allow a reduction in overall geometric footprint compared to conventional high-aspect ratio wings,

while preserving a satisfactory level of aerodynamic efficiency compatible with the mission requirements.

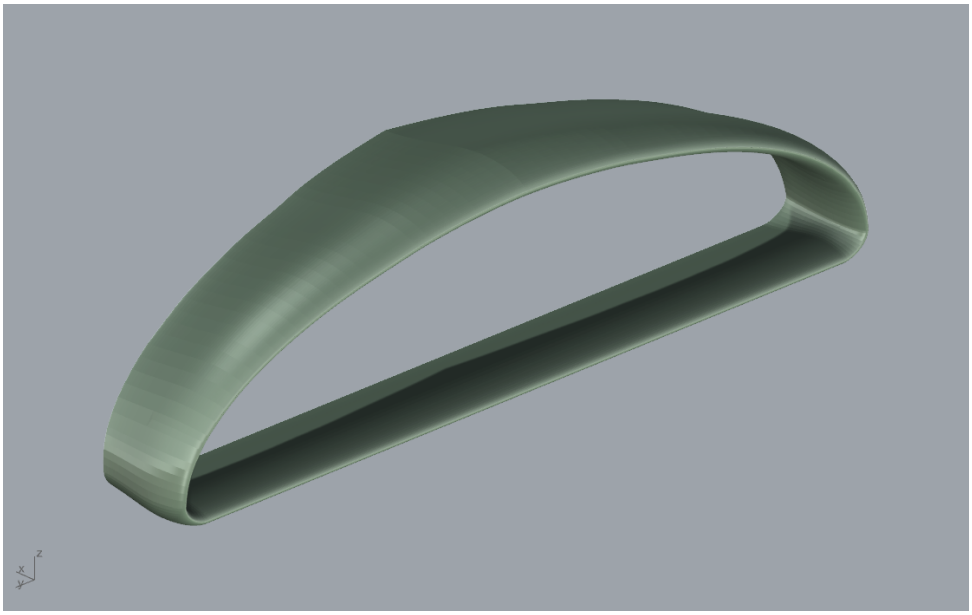


Figure 1 – Hybrid closed-wing HAPS configuration considered in this study.

Despite these promising results, conceptual design and aerodynamic analyses of this hybrid HAPS have, so far, relied on rigid geometries [17]. While this assumption is generally acceptable for conventional aircraft, it represents a critical limitation when applied to inflatable lifting systems. The adoption of inflatable wings makes it necessary to introduce multidisciplinary design approaches from the early project phases, due to the strong coupling between structural behaviour and aerodynamic performance. Unlike traditional airships, which are typically characterized by standard ellipsoid-like aerodynamic bodies, pressure differentials acting on hybrid HAPS structures may induce significant departures from the nominal aerodynamic shape. These deformations can modify fundamental geometrical properties of the wing, such as wingspan, aspect ratio, and airfoil shape, leading to the following consequences:

- Carrying the aerodynamic design exclusively taking into account the nominal geometry can lead to non-negligible deviations in the estimation of performance, thus jeopardizing the definition of the mission profile.
- Pressure differentials directly affect the outer aerodynamic shape. The choice of pressure differentials depends on the mission profile which is in turn dependent on aerodynamic performances.
- Due to the inherent nonlinearity of the structure, change in the structural design and/or pressure differentials might lead to unexpected variations in the pressurized aerodynamic shape and/or structural stiffness.

Such considerations are part of a broader multidisciplinary picture involving more disciplines (e.g., mass & balance, aeroelasticity, subsystem design and flight dynamics). Integrating these domains into a preliminary design cycle represents a primary challenge in the design of such platforms, especially for ensuring compliance with certification requirements. A representative example of this integrated design cycle is illustrated in Figure 2.

2. Scope and Objectives of the Present Work

The present work aims to address some of the aforementioned design challenges by overcoming a key limitation of the current conceptual design approach for hybrid inflatable HAPS, namely the lack of consistency between structural pressurization effects and aerodynamic performance evaluation.

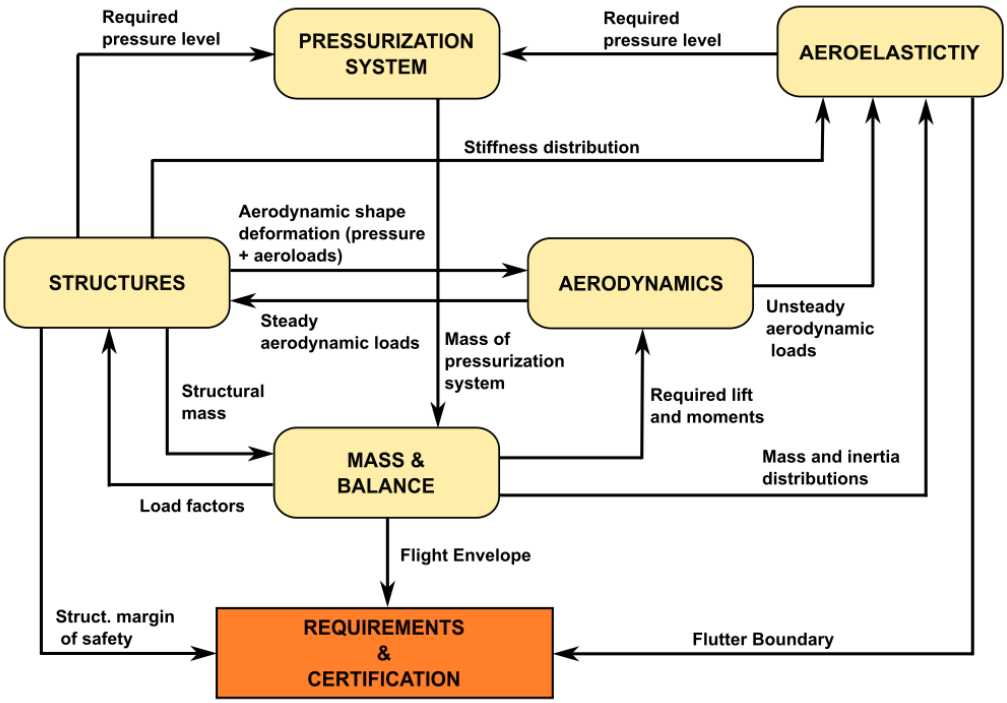


Figure 2 – Example of multidisciplinary design cycle for an inflatable hybrid HAPS.

To this end, a multidisciplinary analysis approach is introduced, coupling the pressurization analysis of a closed-wing inflatable structure with high-fidelity aerodynamic simulations.
Using the explicit solver of LS-DYNA, a pressurization analysis is first performed on a global finite-element model of the platform, to determine the equilibrium geometry of the wing system under different internal pressure conditions, representative of realistic operational scenarios.
The resulting pressure-dependent surfaces are then adopted as reference shapes for the aerodynamic characterization, enabling a physically consistent evaluation of the effects of pressurization on aerodynamic performances and stability characteristics. In detail, the high-fidelity aerodynamic analyses are carried-out to derive the main static aerodynamic curves and performance metrics for both the nominal (rigid) and pressurized configurations, namely: lift curves $C_L(\alpha)$ and corresponding lift-curve slope C_{L_α} in the linear regime, drag polars $C_D(C_L)$ and the associated aerodynamic efficiency L/D as a function of α and longitudinal pitching moment curves $C_M(\alpha)$, used to assess the existence of trim points and local longitudinal static stability in the vicinity of the cruise operating condition. Finally, multiple envelope pressure differentials are studied in order to evaluate the sensitivity of aerodynamic performance and trim behaviour to pressurization-induced shape modifications.
By explicitly accounting for the pressurization-induced shape change and its impact on aerodynamic behaviour, the proposed approach provides a more realistic assessment of the feasibility and performance of hybrid closed-wing HAPS. This methodology represents a step forward toward bridging the gap between early-stage conceptual design and the evaluation of realistic operational configurations for inflatable stratospheric platforms.

3. Description of the Analyzed Configuration and Overview of the Computational Method

The current effort builds upon the work of Riccio *et al.* [17] which proposes the preliminary sizing of a closed-wing HAPS configuration, together with its aerodynamic characterization and stability assessment. The wing system, shown in Figure 1, consists of a lower rectangular wing with zero dihedral angle, whose tip is connected to an upper wing characterized by a gradual negative dihedral. The upper wing exhibits a smooth tapering from the root toward the tip, where it joins the lower wing, resulting in a continuous closed-wing layout. The wing system features Eppler E186 airfoils, with a thickness ratio of 18%, on both wings and the joint. The current work represents the first

systematic effort to tackle the structural design of such configuration, introducing some selected internal components.
Figure 3 shows the internal structural arrangement of the closed-wing HAPS. The external envelope, corresponding to the aerodynamic outer surface of the wing, is realized in fabric and is subjected to a pressure differential. The wing features evenly spaced fabric ribs along the span of both upper and lower wings to transfer aerodynamic loads from the envelope to the spars while limiting deformations of the nominal aerodynamic shape, induced by pressurization. Three conical spars are adopted as the primary shear-carrying elements. These fabric components form an independent pressurized chamber with respect to the external envelope. They are pressurized using a dedicated pressure differential, which can be adjusted to provide additional structural stiffness to the wing and to counteract the effects of envelope pressurization, thereby limiting deviations from the nominal design configuration. Longitudinal struts, connecting the spars, are used to maximize this effect and avoid shrinking in the chord direction of the airfoil, when the envelope is pressurized. The outer surface of the joint connecting upper and lower wing is manufactured from a carbon fiber–based composite, in order to limit local deformations due to pressurization that might compromise aerodynamic performances.
More details concerning the structural properties of these components and the adopted materials are provided in the following section.

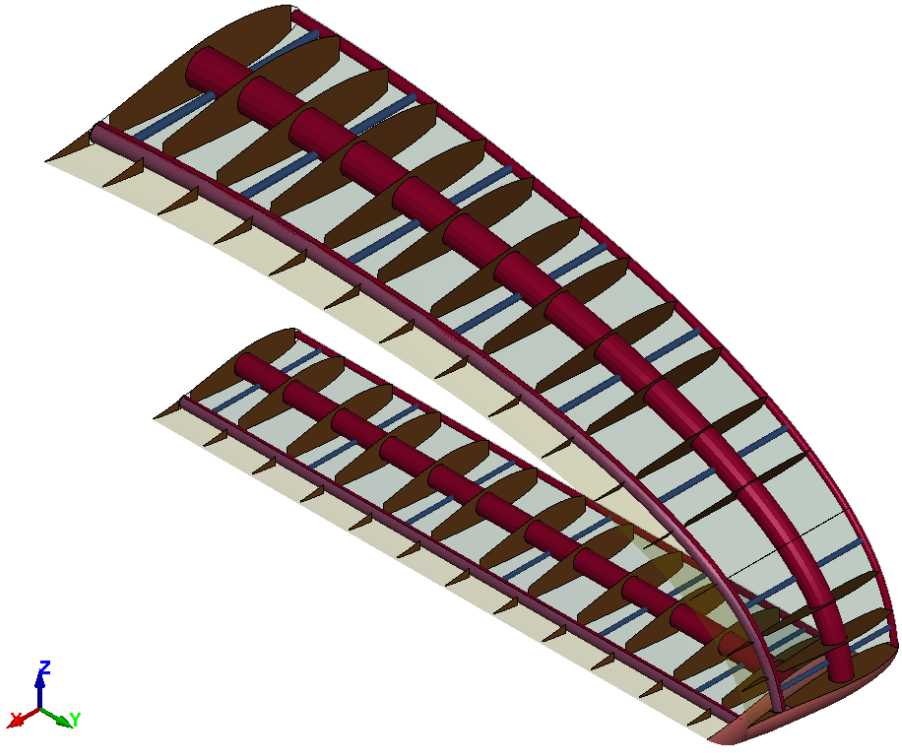


Figure 3 – Visualization of the internal structural arrangement of the closed-wing HAPS configuration considered in this study, as obtained from the FEM model.

3.1 FEM Model and Pressurization Analysis Setup

In this section the structural Finite Element Method (FEM) model of the HAPS is described, along with the methodology adopted to perform pressurization analyses. Given the inherently nonlinear nature of such analyses, mostly influenced by large displacements, contact types and material models, the explicit solver of the commercial software LS-DYNA [18] is selected. This code provides a particularly suitable framework for simulating the behavior of structures incorporating fabric materials and complex nonlinear contact interactions [19, 20]. The analysis is carried out in the time domain: loads, in the form of surface pressures, are progressively applied to the various components, and the solution (in terms of displacements) is evaluated once the transient phase has decayed. This can be easily determined monitoring the system's and kinetic energy. The structural model, whose overview

is presented in Figure 3, can be divided into the following main assemblies, described in detail below and illustrated in Figure 4:

- Envelope and joint
- Spars and struts
- Ribs

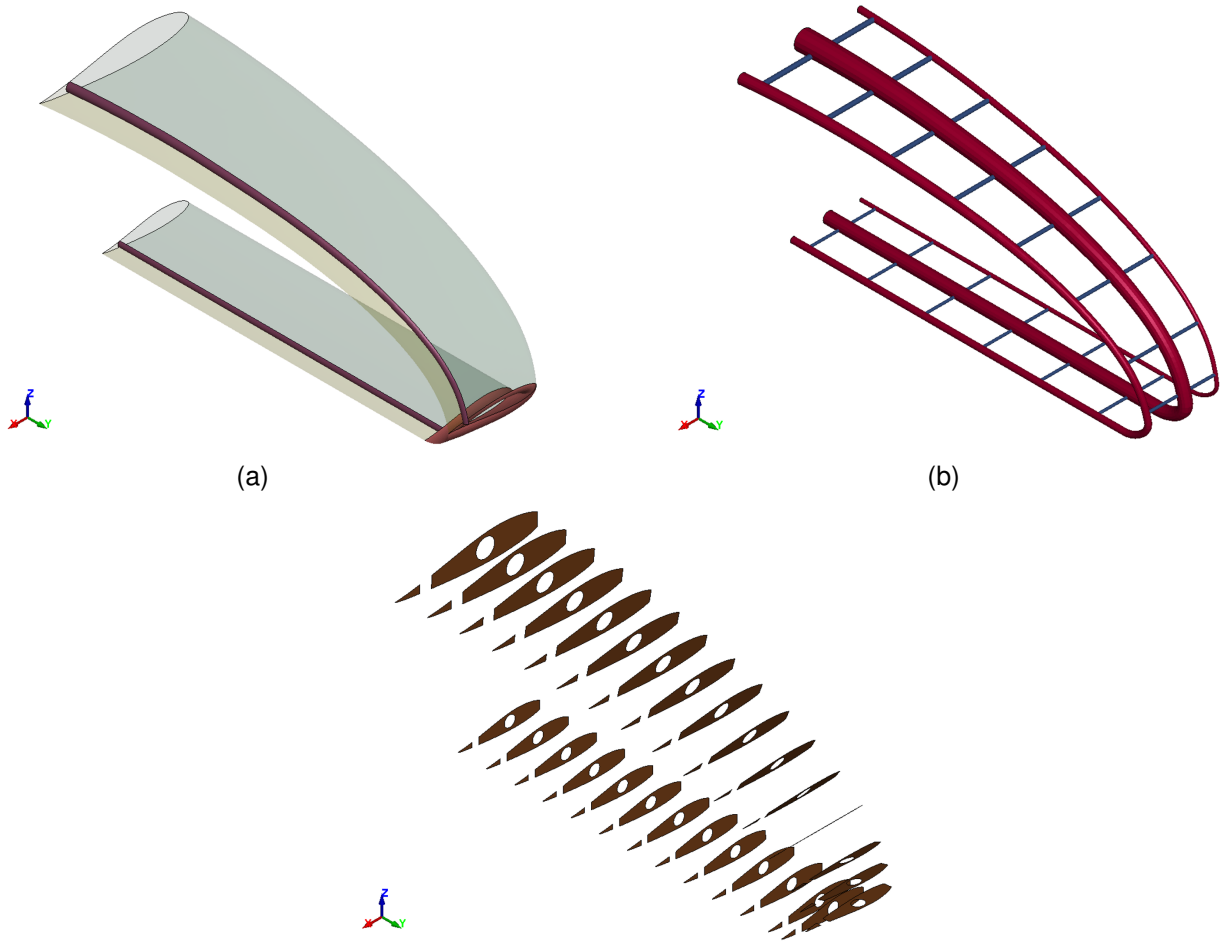


Figure 4 – Structural FEM model main assemblies: (a) envelope and joint, (b) spars and struts, (c) ribs.

Both the geometry and the pressurization loads are symmetric with respect to the XZ plane shown in Figure 3, therefore only half of the configuration needs to be modeled, with symmetry constraints applied to the nodes on the symmetry plane.
The envelope assembly is composed by the envelope (leading and trailing edges) and a wrap, connecting the upper and lower surfaces of the envelope around the rear spar. It is made of fabric and is discretized using *membrane* elements based on the fully integrated Belytschko-Tsay formulation. The joint is part of the envelope connecting upper and lower wings, it extends from leading to trailing edge and features the nominal aerodynamic shape of the wing at the given location. It is modeled with a simplified, composite-inspired material representation and discretized using *shell* elements based on the Belytschko-Lin-Tsay formulation.
For what concerns the spars assembly, the three spars (leading edge, central and rear) are made of fabric and discretized using *membrane* elements based on the fully integrated Belytschko-Tsay formulation, whereas the struts, same as the joint, are modeled with a simplified, composite-inspired material representation and discretized using *shell* elements based on the Belytschko-Lin-Tsay formulation.

Ribs are entirely made of fabric and are discretized using membrane elements based on the fully integrated Belytschko-Tsay formulation. For each rib, the trailing-edge portion defining the geometry of the selected airfoil, is separated from the main rib body in order to accommodate the rear spar as well as the wrapping element connecting the upper and lower sections of the envelope (see Figure 4). The fabric surfaces of the skin and spar groups are made of Dyneema Cuben Fiber CT1E.08, whose principal mechanical properties, as declared by the manufacturer, are listed in Table 1. The adopted material model is the fabric model implemented in the LS-DYNA solver (`*MAT_034/MAT_FABRIC`). This formulation, specifically developed for materials such as fabrics and airbags, allows the user to define engineering stress–strain and shear–strain curves.

Entity	**Value**
Young modulus	8.38 GPa
Shear modulus	3.22 GPa
Ultimate load	552 N / 5 cm
Elongation at break	2.6 %
Density	33 g/m^2
Thickness	50 μm

Table 1 – Mechanical properties and relevant quantities for the Dyneema Cuben Fiber CT1E.08

For composite materials, this characterization can be extended to all necessary in-plane directions of the 2D elements. Cuben Fiber is characterized by two principal fiber orientations, arranged orthogonally. In the absence of detailed information regarding the cutting and bonding of the fabric panels, the modeling focused on achieving the most regular mesh possible, using quadrilateral elements aligned with the principal reference axes. An example of the implemented stress–strain curve is shown in Figure 5, featuring a slope equal to the Young's modulus reported in Table 1 for positive strains and a minimal slope for negative strains, to reproduce the typical compressive behaviour of fabrics while avoiding numerical instabilities.

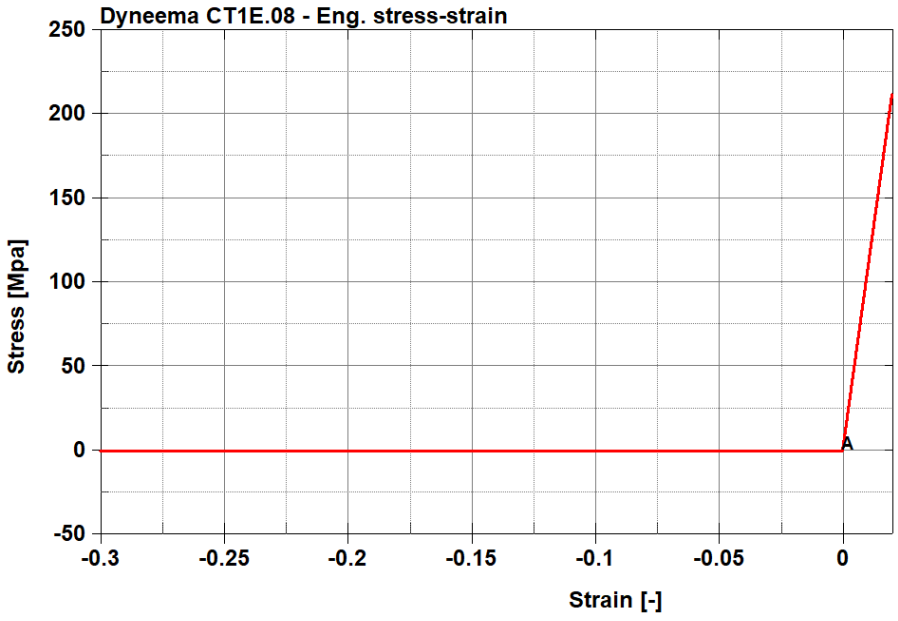


Figure 5 – Engineering stress-strain curve of the Dyneema CubenFiber CT1E.08 implemented in the structural solver.

Considering the early maturity of the project, the joints and struts are modeled using a simplified, isotropic, composite-inspired material description, with properties selected to be representative of

typical aerospace carbon fabrics and to ensure an adequate stiffness of these components as opposed to the Dyneema CubenFiber parts, rather than to capture detailed composite behavior. The properties of such material model are shown in Table 2.

Entity	**Value**
Young modulus	115 GPa
Poisson coeff.	0.23
Density	1.6 g/cm^3
Thickness	5 mm

Table 2 – Mechanical properties and relevant quantities for the composite-inspired material for the joint and struts.

Contacts are used to model the interactions between components of the various assemblies, reproducing the mechanical constraints imposed by the manufacturing and assembling processes. These interactions represent one of the main sources of nonlinearity in the problem. The implementation is carried out using the contact algorithms available in the LS-DYNA solver, calibrated according to the type of interaction and the relative mesh density of the involved parts. A list of the main contacts and their respective types is provided below and illustrated in Figure 6:

- Contact between envelope and spars: mainly concentrated along the leading edge and throughout the length of the rear spar. The contact is of the surface-to-surface type and implemented using the `*CONTACT_AUTOMATIC_SURFACE_TO_SURFACE` algorithm (see Figure 6 (a)).
- Contact between spars and ribs: the ribs are free to slide along the spars. This interaction is modeled as an edge-to-surface contact type, implemented using the `*CONTACT_AUTOMATIC_SURFACE_TO_SURFACE` algorithm (see Figure 6 (b)).
- Tied contact between ribs and envelope: ribs are bonded to the envelope assembly on both upper and lower sides of the wings. This contact is modeled as a tied contact implemented using the `*CONTACT_TIED_NODES_TO_SURFACE` constraint-based algorithm (see Figure 6 (c)).
- Tied contact between struts and spars: the connection between struts and spars has not been modeled in detail for this global preliminary analysis and their fixed connection has been modeled by means of a tied contact by means of the `*CONTACT_TIED_NODES_TO_SURFACE` constraint-based algorithm (see Figure 6 (d)).

Table 3 summarizes the main properties of the FEM model .

Entity	**Value**
Element nr.	93284
Node nr.	95346
Minimum time-step [s]	3.48E-07

Table 3 – Main properties of the FEM model used for pressurization analyses.

To model the pressure differentials in the various chambers, surface loads are applied to the elements of the spars and envelope assemblies. These loads are introduced through a ramp-like profile, calibrated to prevent numerical instabilities while allowing the transient response to decay quickly. Mass-proportional damping is used to suppress the system's oscillatory response, thereby reducing the simulated physical time required to reach the steady-state equilibrium condition.
Two load cases, summarized in Table 4, are investigated in this work, each characterized by a distinct set of pressure differentials across the chambers. These values are selected based on preliminary

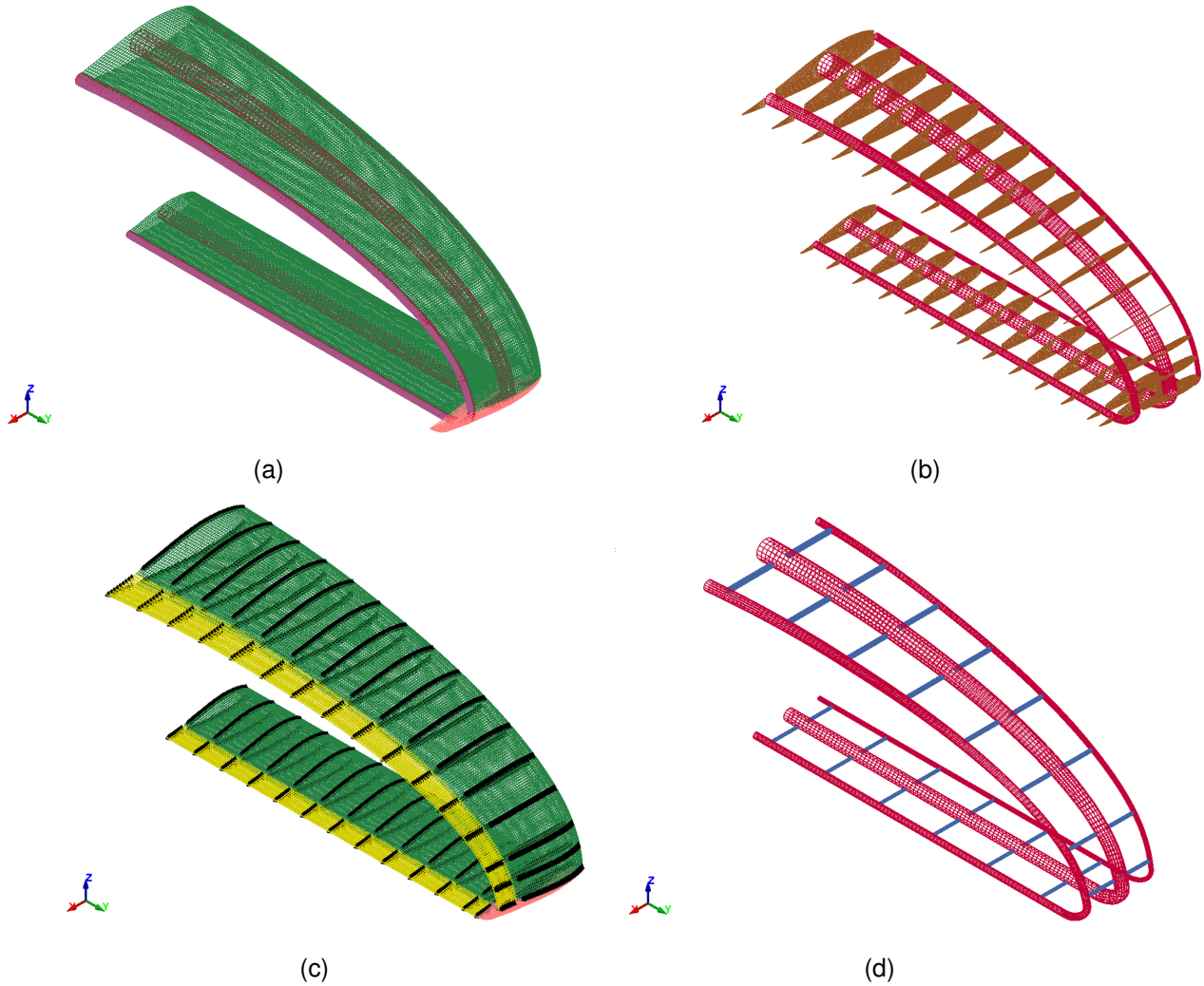


Figure 6 – Structural FEM model: main contact types. (a) contact between envelope and spars, (b) contact between spars and ribs, (c) Tied contact between ribs and envelope, (d) tied contact between struts and spars.

internal stress assessments for structural integrity and on design know-how developed for similar configurations currently under development.

The choice of the spars pressure differential stems from multiple considerations. As a first approximation, the upper bound is governed by the hoop stress of the central spar. For a thin-walled cylinder, this is defined as:

$$\Delta p_{\max} = \sigma_{\text{ult}} \cdot t / R \tag{1}$$

where $R = 0.490$ m is the maximum radius of the central spar at the upper wing root section and σ_{ult} is the ultimate stress of the Dyneema CT1E.08 fabric (Table 1). This yields a maximum theoretical pressure $\Delta p_{\max}$ of 11000 Pa. In practice, operational values must account for a standard regulatory safety factor of 1.5 and match the performance envelope of the pressurization system. Pressure differentials of 6000 Pa are currently under evaluation for this type of hybrid configurations. This baseline choice successfully satisfies structural stiffness requirements while compatible with compressors design with weight and performance (such as mass flow rate, and power) compatible with HAPS mission profiles, across all flight phases.

Regarding boundary conditions, in addition to the symmetry constraints applied on the XZ plane (see Figure 3), the leading edge of the lower wing airfoil located on the symmetry plane is clamped to suppress rigid-body motions. This combination of constraints is thought to allow realistic deformation of the airfoils, as well as relative motion between the upper and lower wings about the nominal configuration, following pressurization.

Chamber	Nominal pressure differential	
	Load Case 1	Load Case 2
Envelope	250 Pa	350 Pa
Spars	6000 Pa	6000 Pa

Table 4 – Load cases with nominal pressure differentials (with respect to external atmosphere) for the different chambers.

3.2 Aerodynamic analysis setup

The aerodynamic analysis is performed on three different geometric configurations of the platform: the nominal CAD geometry, previously adopted in earlier studies, assuming a rigid, undeformed structure [17], and two pressurized configurations corresponding to envelope pressure differentials of 250 Pa and 350 Pa, obtained from the pressurization analyses described in the previous section. In order to enable a consistent and meaningful comparison, the numerical setup, turbulence modeling, computational domain, mesh generation strategy, and boundary conditions are kept identical for all cases. Considering that comparable levels of numerical convergence are ensured for all simulations and that the geometric modifications induced by the pressurization process are limited to local deformations, without altering the overall topology of the lifting system, differences observed in the aerodynamic coefficients can be expected to be primarily attributed to the geometry changes resulting from pressurization.

The aerodynamic simulations are carried out using the steady-state, incompressible Reynolds-Averaged Navier–Stokes (RANS) solver `simpleFoam` implemented in OpenFOAM, coupled with the k–ω SST turbulence model. The computational domain adopted for the RANS simulations is shown in Fig. 7. With the maximum wing chord $c = 7.8$ m taken as reference length, the domain consists of a three-dimensional volume surrounding the configuration, with the inlet boundary positioned approximately $15c$ upstream of the configuration's center of gravity and the outlet boundary located approximately $46c$ downstream. The lateral and vertical far-field boundaries are placed at distances of approximately $28c$ from the configuration's center of gravity. Such domain dimensions are selected to minimize spurious blockage and boundary-interference effects while ensuring numerical stability for the investigated angles of attack. Turbulence quantities are initialized assuming a free-stream turbulence intensity of 5%. The turbulent kinetic energy is computed as

$$k = \tfrac{3}{2}(VI)^2,$$

which, for a freestream velocity $V = 16$ m/s and turbulence intensity $I = 0.05$, yields $k = 0.96$ m^2/s^2. The specific dissipation rate is set to $\omega = 600.41$ s^{-1}, corresponding to a turbulence viscosity ratio $\mu_t/\mu = 10.0$. Wall treatment functions are not employed, as the computational mesh is refined to maintain $y^+ < 1$ over all solid surfaces. The viscous sublayer is therefore directly resolved through appropriate inflation layer modelling. Standard wall functions are retained in the solver setup exclusively to enable the evaluation of the y^+ field, but they remain inactive throughout the simulations. Convergence is ensured by reducing the residuals of all governing equations below 10^{-4}. The initial turbulence model parameters are summarised in Table 5.

Table 6 summarises the boundary conditions applied to the velocity, pressure, and turbulence fields for the reference RANS simulation at an angle of attack $\alpha = 0^\circ$ and sideslip angle $\beta = 0^\circ$.

The CFD analysis is conducted to evaluate the flow field around the platform and to obtain accurate evaluation of the aerodynamic coefficients. Simulations are performed at an altitude of 20 km with a freestream velocity of 16 m/s. The angle of attack is varied in the range -15° to 22°, while the sideslip angle β is set to 0°.

An unstructured aerodynamic mesh of the platform and surrounding domain is generated using Ansys mesher. The mesh consists of prismatic inflation layers near the solid surfaces and tetrahedral elements in the far field, resulting in approximately 15×10^6 cells and 5×10^6 nodes. For completeness, the resulting surface unstructured mesh of the inflated closed-wing configuration corresponding to an

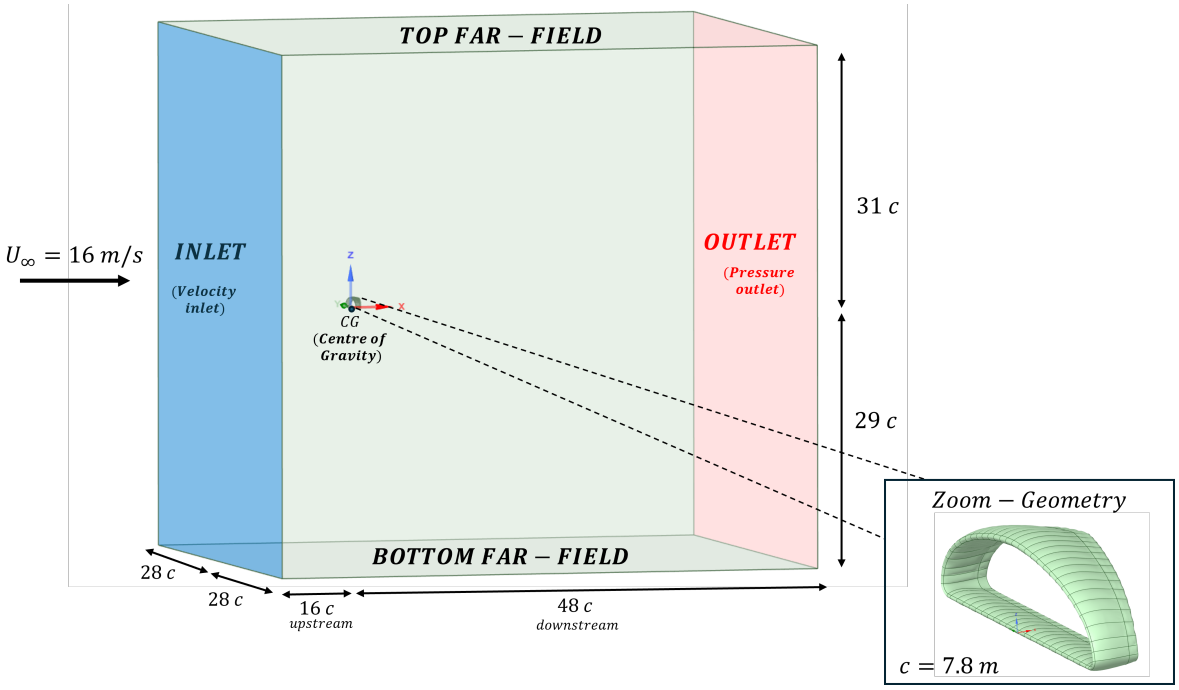


Figure 7 – Computational domain adopted for the CFD analyses, including inlet, outlet, and far-field boundaries. The reference chord is $c = 7.8$ m.

Parameter	Value
Turbulence intensity I	5%
Turbulent kinetic energy k	$0.96\ \mathrm{m}^2/\mathrm{s}^2$
Specific dissipation rate ω	$600.41\ \mathrm{s}^{-1}$
Turbulence viscosity ratio μ_t/μ	10.0
Wall treatment	$y^+ < 1$ (no wall functions)
Convergence criterion	Residuals $< 10^{-4}$

Table 5 – Initial turbulence model parameters used in the RANS simulations. From Riccio *et al.* [17].

Field	Boundary condition	Physical meaning
Velocity U (inlet)	`fixedValue` $(16,\ 0,\ 0)$ m/s	Freestream velocity
Velocity U (outlet)	`inletOutlet`	Mixed inflow/outflow condition
Pressure p (inlet)	`zeroGradient`	Zero normal gradient
Pressure p (outlet)	`fixedValue` $(0$ Pa$)$	Reference pressure
Turbulence k, ω (inlet)	`fixedValue` (Table 5)	Freestream turbulence values
Turbulence k, ω (outlet)	`inletOutlet`	Mixed inflow/outflow condition
Solid surfaces	$y^+ < 1$, wall functions deactivated	No wall-function modelling

Table 6 – Boundary conditions adopted in the RANS simulations for $\alpha = 0°$ and $\beta = 0°$. From Riccio *et al.* [17].

envelope pressure differential of 250 Pa is shown in Fig. 8. The same meshing strategy is applied to the 350 Pa inflated configuration.

The boundary layer resolution is designed according to the flow conditions and platform geometry. Assuming a target value of $y^+ = 1$, the initial inflation layer height is set to 1×10^{-4} m, with a maximum

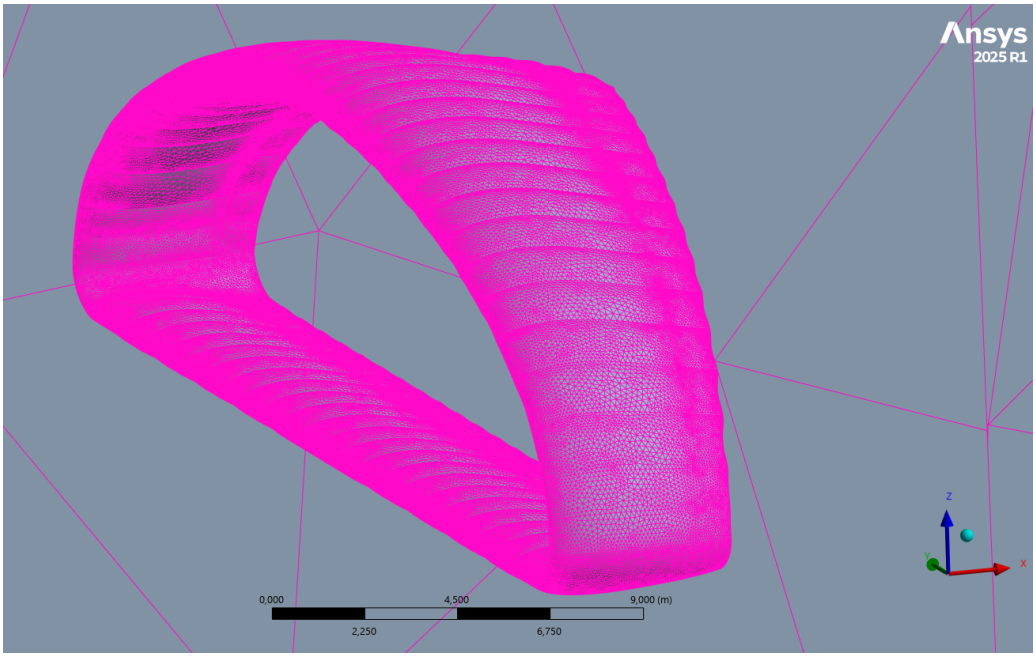
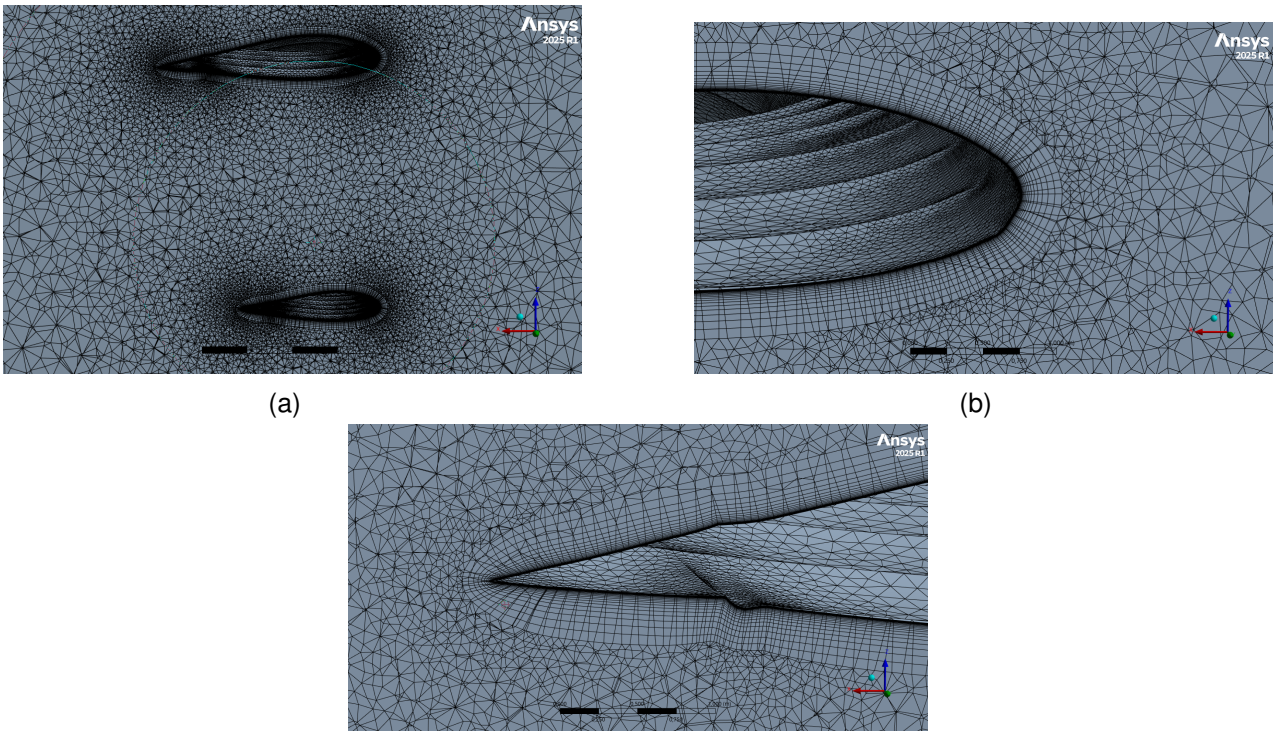


Figure 8 – Unstructured aerodynamic surface mesh of the 250 Pa pressurized closed-wing configuration adopted as reference for the aerodynamic analyses.

number of 30 layers and a growth rate equal to 1.25. The resulting inflation layers for the reference mesh are shown in Fig. 9. Since the inflated geometries preserve the same overall topology and characteristic length scales, and the same meshing strategy is applied, the selected mesh resolution is considered adequate also for the pressurized configurations.



(a) (b)

(c)

Figure 9 – Boundary-layer inflation layers adopted in the aerodynamic mesh of the 250 Pa pressurized closed-wing configuration: (a) X–Z plane view; (b) leading-edge zoom; (c) trailing-edge zoom.

4. Results

4.1 Results of the Pressurization Analyses

Pressurization analyses are executed by progressively applying surface pressures to the envelope and spars assemblies, in accordance with the values of the load cases listed in Table 4. Steady-state equilibrium is achieved at the conclusion of the transient phase after the system's kinetic energy has decayed to zero. Figure 10 shows the system's kinetic energy evolution over time for the two load cases. It can be noted how, the kinetic energy reaches its maximum during the loading phase and gradually diminishes to zero during the subsequent transient phase, due to the adopted mass-proportional structural damping.

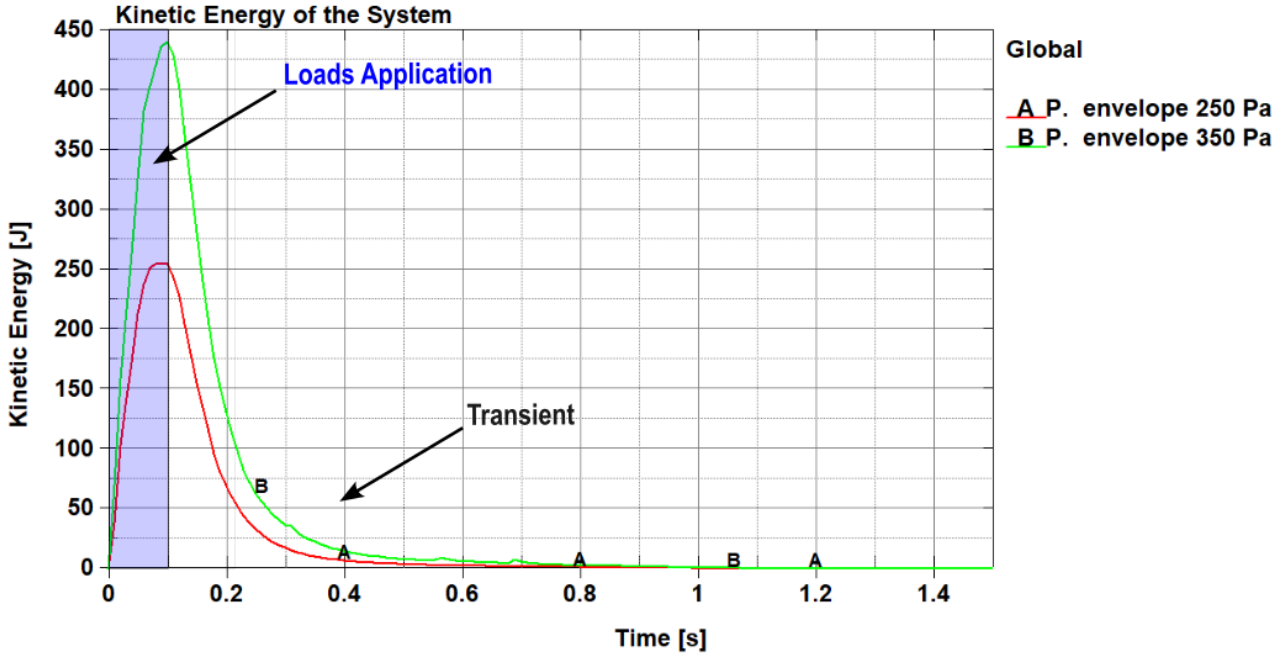


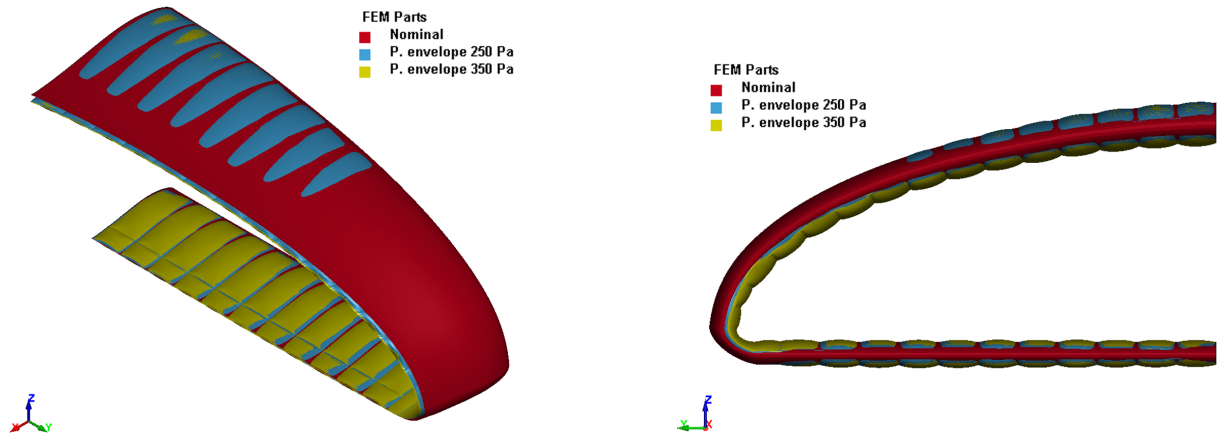
Figure 10 – Pressurization analyses: evolution of system's kinetic energy for the two studied load cases.

A comparison between the pressurized configurations corresponding to the load cases listed in Table 4, and the nominal shape is presented in Figure 11, with particular emphasis on the envelope, i.e., the outer aerodynamic shape of the platform. The nominal shape of the Eppler E186 is only retained at rib stations, where it is strictly enforced by the ribs themselves. Between these stations, however, the pressurized configurations exhibit an increase in the thickness of the nominal airfoil shapes on both wings, with the magnitude of this increase being proportional to the applied envelope pressure differential.

A further evident effect of pressurization is a reduction in the overall wingspan: the joint, while maintaining its orientation relative to the two wings, shifts toward the symmetry plane by an amount proportional to the imposed pressure differential. This behavior is clearly illustrated in Figure 12, which shows the evolution of the wing semi-span, measured at the joint leading edge, during pressurization, for the two load cases. By the time steady-state equilibrium is reached, the wingspan is reduced by approximately 1.35% and 1.95% for the envelope pressures of, respectively, 250 and 350 Pa.

Closely related to this effect is the modification of the upper wing dihedral in the vicinity of the joint, as illustrated in Figure 11 (b). It appears as if, under pressurization, the structure tends to reduce the nominal pronounced curvature present in the upper wing near its connection with the lower wing. This effect, potentially affecting the aerodynamics of the wing tip, depends on the structural layout and can be tuned through appropriate design choices, such as the ribs distribution and the joint geometry.

Figure 13 highlights a few further effects of pressurization that contribute to modifications of the aerodynamic performance of the nominal geometry. In particular, the leading-edge radius of both wings increases as envelope pressurization induces expansion of the airfoil thickness and drives



(a) (b)

Figure 11 – Pressurization analyses: comparison of results: (a) isometric and (b) front views.

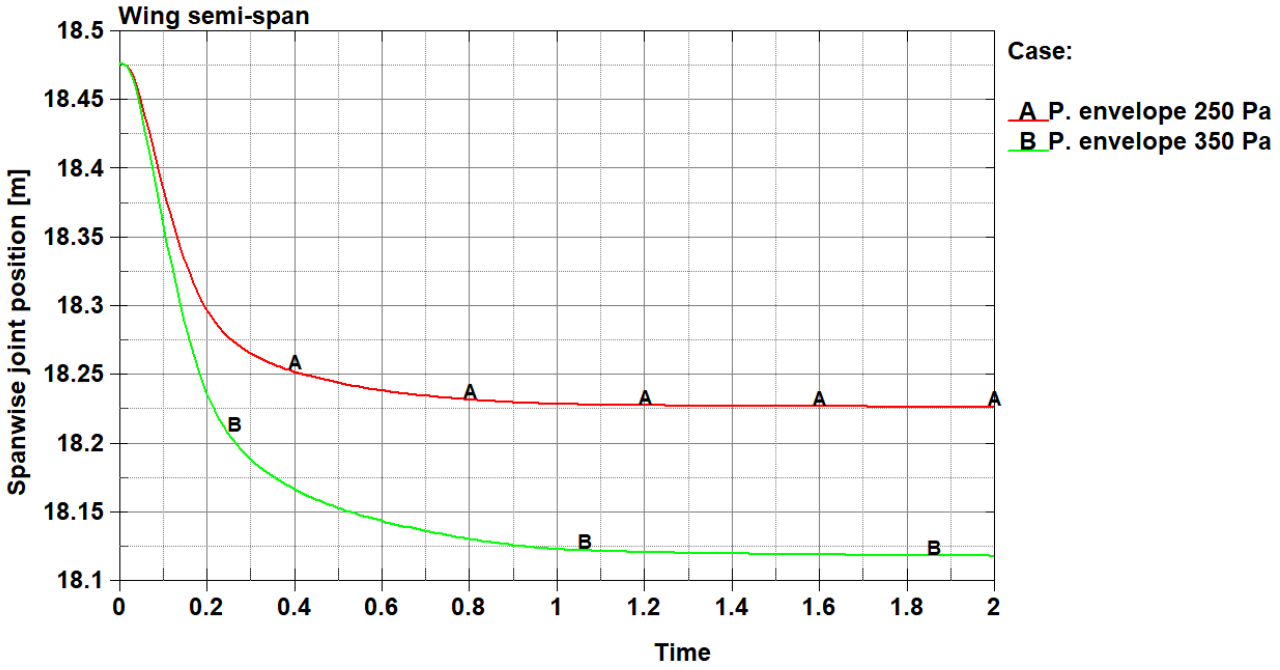


Figure 12 – Pressurization analyses: wing semi-span length variation for the two studied load cases.

the leading-edge spar toward the trailing edge. This behavior is influenced by the internal structural layout, including the number and geometry of the struts.

Last significant effect of pressurization is the modification of the upper wing airfoil shape in the trailing-edge region. The discontinuity of the ribs in this area prevents the preservation of the selected E186 airfoil geometry. As a result, under pressurization, the trailing edge of the upper wing undergoes a downward deflection toward the lower wing, rotating around the rear spar.

The effect of the overall airfoil shape modifications, resulting in airfoil thickening, leading-edge radius expansion, and trailing-edge shape deformation, can be appreciated in Figure 14, which compares the envelope sections of the upper and lower wing roots for the nominal and the two pressurized configurations under investigation. This comparison highlights how these effects scale proportionally with the pressure differential on both wings. Finally, Figure 14 shows how, on the upper wing, pressurization induces a local reorientation of the airfoil, resulting in a shift in its geometric angle of attack. A close look to the upper wing in Figure 13 reveals how this effect is distributed spanwise from root to tip.

Table 7 quantifies the relevant changes in the wing geometry discussed so far, providing data on

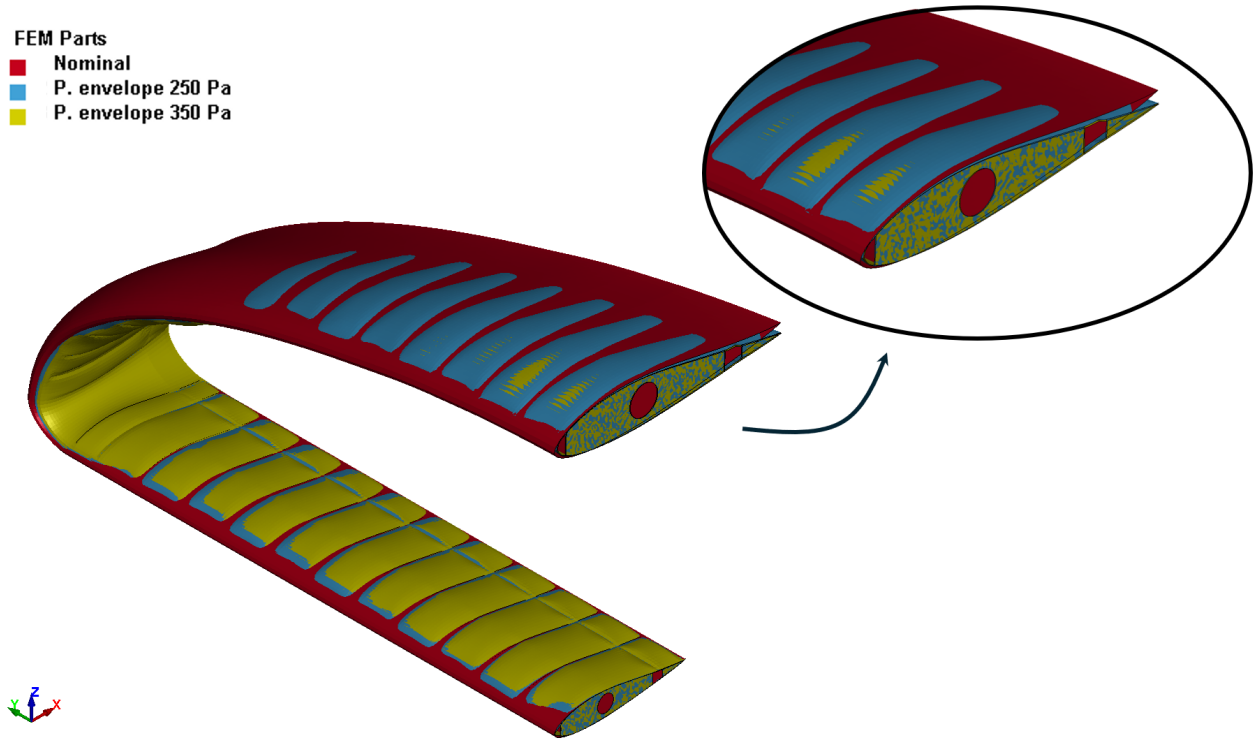


Figure 13 – Pressurization analyses: isometric view of pressurized configurations with detail of the upper wing.

upper and lower wing root sections deformations and span modifications for the pressurized cases.

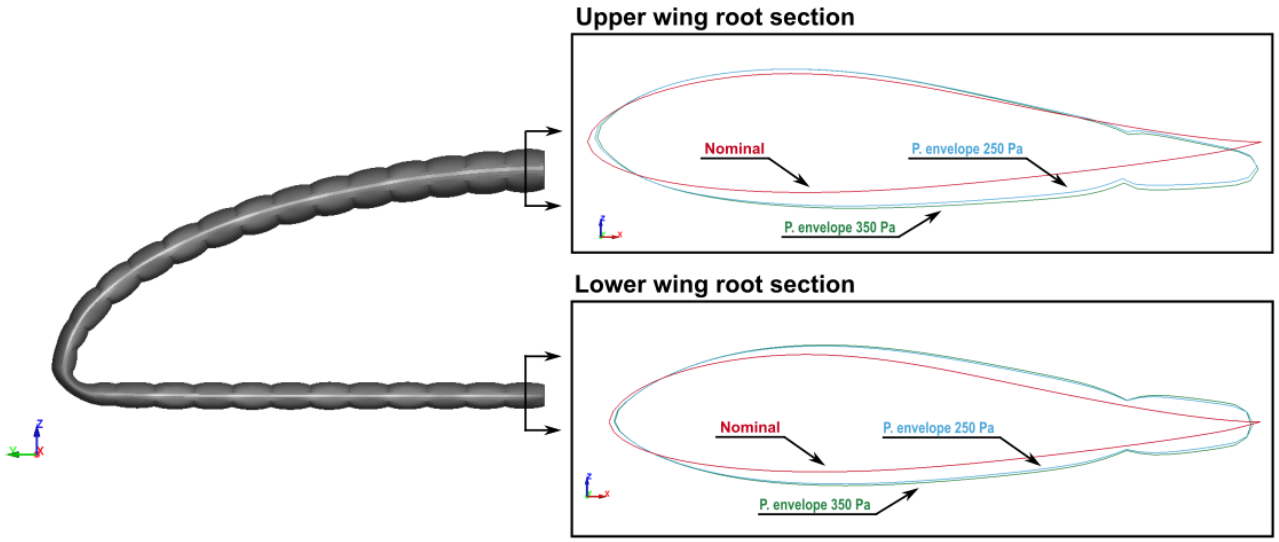


Figure 14 – Pressurization analyses: effects of pressurization on the airfoils geometry. Scaled comparison between the airfoils of the nominal and pressurized configurations for the upper and lower wings root sections.

4.2 Aerodynamic Results on Nominal and Pressurized Configurations

The aerodynamic performance of the hybrid closed-wing HAPS is assessed by comparing the nominal (non-inflated) configuration [17] with the inflated equilibrium geometries obtained from the pressurization analyses with envelope pressure differentials of 250 Pa and 350 Pa, as for the load cases reported in Table 4. When comparing the nominal and inflated configurations, a common reference system is adopted for the definition of the geometric angles of attack and sideslip. In particular, the

		Configuration					
Component	**Parameter**	**Nominal**		**P. 250 Pa**		**P. 350 Pa**	
		Value	Var. wrt Nominal	Value	Var. wrt nominal	Value	Var. wrt Nominal
Lower	t/c [%]	18.0	–	21.3	18.3%	21.8	21.1%
wing root	C [m]	4.626	–	4.543	-1.79%	4.520	-2.29%
section	α_{geo} [deg]	0	–	0.2	–	0.3	–
Upper	t/c [%]	18.0	–	20.8	15.5%	21.1	17.2%
wing root	C [m]	7.862	–	7.735	-1.61%	7.721	-1.79%
section	α_{geo} [deg]	0	–	2.5	–	2.8	–
Wing tip	Semi-span [m]	18.48	–	18.23	-1.35%	18.12	-1.95%

Table 7 – Pressurization analyses: effects of pressurization on airfoils geometry for the upper and lower wing root sections and wingspan. Comparison and percentage variations of pressurized configurations with respect to the nominal one.

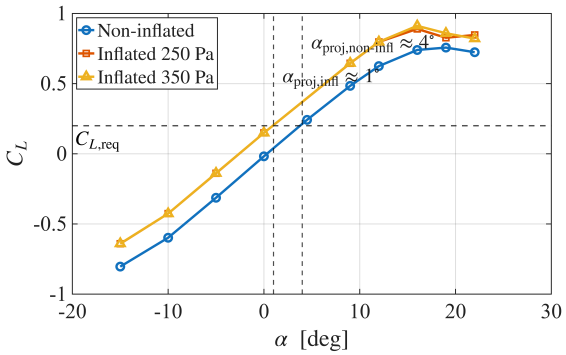
angle of attack α is defined as the geometric angle between the freestream velocity vector and the chord line of the lower wing in the nominal configuration. The comparison focuses on lift characteristics, drag polar, and aerodynamic efficiency at cruise condition.

Figure 15a shows the lift coefficient as a function of the angle of attack. All configurations exhibit an approximately linear lift behaviour over a wide range of angles, with a comparable lift-curve slope C_{L_α} in the linear regime. This indicates that pressurization-induced deformations do not significantly affect the lift sensitivity to angle of attack. However, the inflated configurations show an upward shift of the lift curve, producing higher lift at a given geometric angle of attack. Based on the preliminary sizing conducted in Riccio *et al.* [17], which identifies a preliminary platform mass of approximately 127 kg, at the reference flight condition (altitude $20\ \text{km}$, freestream velocity $V = 16\ \text{m/s}$), the effective aerodynamic load, taking into account buoyancy contributions, is $W_{\text{eff}} = 991.65\ \text{N}$, which yields a required lift coefficient of $C_{L,\text{req}} = 0.200$. By interpolating the CFD lift curves, the corresponding operating angles of attack are found to be $\alpha_{\text{proj}} \approx 4^\circ$ for the non-inflated configuration and $\alpha_{\text{proj}} \approx 1^\circ$ for the inflated configurations. This behaviour is consistent with a pressurization-induced modification of the lifting-system geometry, which increases the relative incidence of the upper wing with respect to the lower-wing chord reference. As shown in Figure 13 the deformation of the rear portion of the upper wing produces an aerodynamic effect that increases lift at a given α. As a result, the inflated geometries reach the required lift coefficient at a significantly lower geometric angle of attack.

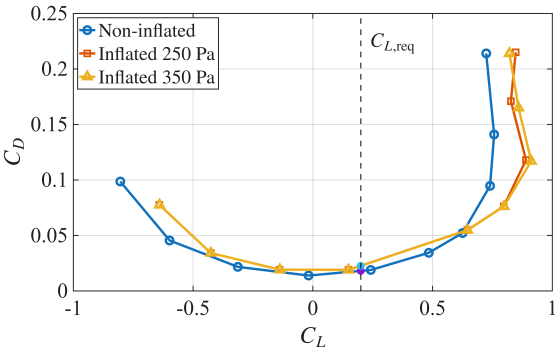
The drag polar comparison reported in Figure 15b indicates an overall drag increase for the inflated configurations over most of the lift range. Specifically, at the required lift coefficient, the inflated configurations at 250 Pa and 350 Pa exhibit drag coefficients approximately 25.4% and 24.9% higher than that of the nominal geometry, respectively.

Figure 15c presents the lift-to-drag ratio as a function of the angle of attack. The non-inflated configuration achieves a slightly higher peak aerodynamic efficiency, whereas the inflated configurations exhibit a reduced maximum L/D. Although all configurations display comparable L/D values in the vicinity of their respective cruise operating points, the inflated configurations operate at a lower angle of attack away from their optimal efficiency condition. As a result, the pressurization-induced shift of the operating point leads to a clear aerodynamic efficiency penalty at the cruise condition.

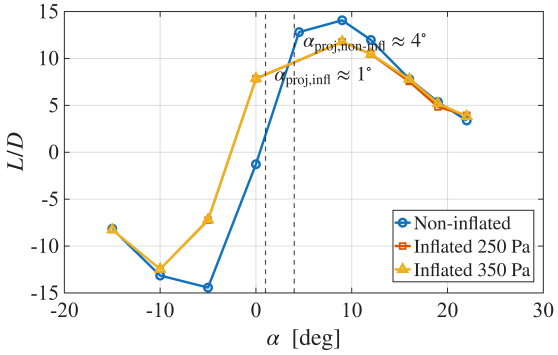
Overall, these results indicate that pressurization induces a shift in the aerodynamic operating point while simultaneously reducing the aerodynamic efficiency. Finally, it can be noted how the differences in the considered aerodynamic coefficients is negligible for pressurization levels in the range between 250 Pa and 350 Pa.



(a) Lift coefficient vs angle of attack.



(b) Drag polar comparison.



(c) Lift-to-drag ratio vs angle of attack.

Figure 15 – Aerodynamic performance comparison between the nominal configuration and the inflated configurations at 250 Pa and 350 Pa. The values of α_{proj} yielding the required lift coefficient $C_{L,\text{req}}$ are shown for all configurations.

4.3 Longitudinal Pitching Moment and Trim Implications

The longitudinal pitching moment plays a central role in determining trim conditions and static equilibrium. Figure 16 compares the total pitching moment coefficient $C_{M,\text{tot}}$ as a function of the angle of attack for the nominal (non-inflated) configuration and the inflated configurations at 250 Pa and 350 Pa. $C_{M,\text{tot}}$ can be expressed as:

$$C_{M,\text{tot}} = C_{M,\text{aero}} + C_{M,\text{buoy}} \tag{2}$$

where $C_{M,\text{aero}}$ is obtained from the CFD calculations and $C_{M,\text{buoy}}$ represents the buoyancy-induced contribution, which, consistently with the work of Riccio *et al.* [17], is modeled using a simplified approach based on the volume of the nominal configuration.

The non-inflated configuration exhibits a statically stable behavior in the vicinity of the cruise operating condition and for positive angles of attack. The pitching moment curve crosses the zero-moment line at approximately $\alpha = 4°$, in agreement with the cruise angle of attack identified from the lift analysis [17]. The negative slope of C_M in the vicinity of this point indicates the presence of a free (or uncontrolled) trim condition and positive longitudinal static stability.

On the other hand, the inflated configurations exhibits a similar qualitative trend of the pitching moment curve, but shifted toward negative values over the entire investigated angle-of-attack range. No zero-crossing of the curve is in fact observed for either pressurized configuration. At angle of attack $\alpha_{proj} \approx 1°$ yielding the required lift coefficient $C_{L,\text{req}}$ (see Fig. 15), the pitching moment remains significantly negative, with values of approximately $C_M = -0.0185$ for both pressurized configurations, indicating a persistent nose-down tendency. The results also show only limited differences between the 250 Pa and 350 Pa configurations, suggesting that the dominant effect stems from the transition from the nominal to the pressurized shape, rather than from further geometry variations within the investigated pressure range.

It is worth noting that the total pitching moment coefficient $C_{M,\text{tot}}$ reported in Fig. 16 includes the

buoyancy-induced contribution $C_{M,\text{buoy}}$ (see Equation 2). For the nominal configuration, this contribution shifts the pitching moment curve downward, moving the natural trim point to the cruise condition at $\alpha \approx 4°$. For the pressurized configurations this same effect appears to operate synergistically with the pressurization-induced deformations causing the zero-crossing to disappear entirely within the investigated angle-of-attack range. In conclusion, the results suggest that the pressurization-induced deformations, such as those shown in Figure 13 and Figure 14, alter the pressure distribution over the wing system, producing an additional nose-down pitching-moment contribution and consequently shifting the longitudinal pitching-moment curve toward more negative values.

From a design standpoint, this implies that the pressurized configurations cannot achieve longitudinal trim passively. Active pitch control or permanent control surface deflections would therefore be required to maintain equilibrium. Beyond the impact on aerodynamic efficiency, pressurization exerts a critical influence on trim and stability, which must be directly accounted for in the design of inflatable closed wing hybrid HAPS platforms.

These results underline how carrying the aerodynamic design exclusively taking into account the nominal geometry can lead to non-negligible deviations in the estimation of performances, and they reinforce the assumption that a multidisciplinary approach is essential starting from early design stages for the synthesis of the configuration.

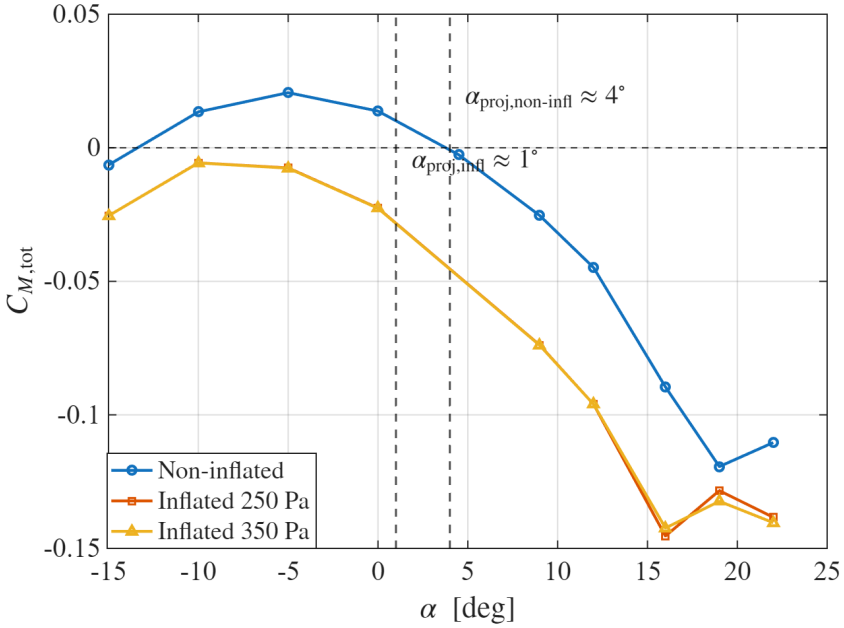


Figure 16 – Total pitching moment coefficient as a function of angle of attack for the nominal configuration and the inflated configurations at 250 Pa and 350 Pa. The values of α_{proj} yielding the required lift coefficient $C_{L,\text{req}}$ are shown for all configurations.

5. Conclusions

This work presented a multidisciplinary structural-aerodynamic characterization of a novel hybrid closed-wing HAPS configuration, aimed at improving traditional early-stage conceptual design methodologies with a higher-order multidisciplinary characterization. The study clearly demonstrated how, for inflatable hybrid platforms, the strong coupling between internal pressurization and aerodynamic shape represents a first-order design driver that cannot be neglected in the assessment of aerodynamic performances.

To address this coupling, a high-fidelity computational framework was established. A nonlinear global finite-element model of the platform was developed in LS-DYNA to simulate the structural equilibrium of the fabric envelope, internal spars, and other relevant structural components under different pressurization load cases. The resulting pressurized aerodynamic shapes were subsequently used as the basis for high-fidelity RANS CFD simulations in OpenFOAM, allowing a direct performance comparison against the nominal, rigid CAD geometry.

Two pressure load cases were considered, corresponding to envelope pressure differentials of 250 Pa and 350 Pa with a constant spar pressure differential of 6000 Pa. The pressurization analyses revealed significant deviations from the nominal design shape, with overall changes in the airfoil shape at all sections between ribs, including overall increase in airfoil thickness and in the leading-edge radius, a reduction in total wingspan as the joint region shifted toward the symmetry plane, and a trailing-edge downward deflection on the upper wing.

These pressurization-induced geometric changes resulted in significant shifts in aerodynamic performance and stability. While the lift-curve slope C_{L_α} remained comparable across all configurations, the inflated geometries exhibited an upward shift of the lift curve, allowing the required cruise lift coefficient $C_{L,\text{req}}$ to be achieved at a significantly lower angle of attack ($\alpha_{\text{proj}} \approx 1^\circ$ versus 4° for the nominal configuration). However, this shift was accompanied by a drag increase of approximately 25% at the operating point and a corresponding penalty in aerodynamic efficiency. Moreover, the inflated shapes introduced a persistent nose-down pitching moment ($C_{M,\text{tot}} < 0$ over the entire investigated angle-of-attack range), eliminating the passive trim point observed in the nominal geometry and implying the need for active control strategies or dedicated trimming solutions.

Furthermore, the comparison between the 250 Pa and 350 Pa configurations demonstrated that the aerodynamic response is substantially insensitive to variations in the envelope pressure differential within the investigated range, suggesting that the dominant effect is associated with the transition from the nominal to the pressurized shape rather than with the specific adopted pressurization level.

These findings confirm that designing hybrid closed-wing HAPS based solely on nominal geometries leads to non-negligible performance estimation errors, and underscore the necessity of integrated multidisciplinary design methodologies for the successful synthesis of such unconventional platforms.

5.1 Future Works

Future developments will extend the present aerodynamic analysis toward asymmetric flight conditions for various sideslip angles, enabling the generation of complete aerodynamic databases for nominal and pressurized configurations. This will support future investigations on trim, lateral-directional stability and a comprehensive flight-dynamic characterization of this hybrid closed-wing HAPS platform.

Acknowledgments

The activity was carried out within the framework of the *Space It Up* project, funded by the Italian Space Agency (ASI), CUP I53D24000060005.

Copyright Statement

The authors confirm that they, and/or their company or organization, hold copyright on all of the original material included in this paper. The authors also confirm that they have obtained permission, from the copyright holder of any third party material included in this paper, to publish it as part of their paper. The authors confirm that they give permission, or have obtained permission from the copyright holder of this paper, for the publication and distribution of this paper as part of the ICAS proceedings or as individual off-prints from the proceedings.

References

[1] J Gonzalo, D López, D Domínguez, A García, and A Escapa. On the capabilities and limitations of high-altitude pseudo-satellites. *Progress in Aerospace Sciences*, 98:37–56, 2018.

[2] Anthony J Colozza. High altitude propeller design and analysis overview. 1998. NASA Glenn Research Center.

[3] F. Nikodem et al. Overview of the DLR high altitude platform and scientific potential of the technology demonstrator HAP-ALPHA. In *Deutscher Luft- und Raumfahrtkongress (DLRK)*, 2023.

[4] G. Svistunov, A. Akhtarshenas, D. López-Pérez, M. Giordani, G. Geraci, and H. Yanikomeroglu. Bridging earth and space: A survey on haps for non-terrestrial networks, 2026.

[5] Sceye. High altitude platform systems (haps). `https://www.sceye.com/platform`, 2024. Accessed: 2024-02-05.

[6] Adrián Delgado, Diego Domínguez, Jesús Gonzalo, and Alberto Escapa. Station-keeping haps mission through optimal sprint and drift trajectories. *Aerospace Science and Technology*, 152:109365, 2024.

[7] Jiwei Tang, Weicheng Xie, Pingfang Zhou, Hui Yang, Tongxin Zhang, and Quanbao Wang. Multidisciplinary optimization and analysis of stratospheric airships powered by solar arrays. *Aerospace*, 10(1), 2023.

[8] Vincenzo R. Baraniello, Giuseppe Persechino, and Roberto Borsa. Tools for the conceptual design of a stratospheric hybrid platform. *SAE Technical Paper*, 2020-01-0025, 2020.

[9] Vincenzo Rosario Baraniello, Giuseppe Persechino, Cesario Vincenzo Angelino, and Francesco Tufano. The application of high altitude pseudo-satellites for a rapid disaster response. In *2021 IEEE International Geoscience and Remote Sensing Symposium IGARSS*, pages 8400–8403, 2021.

[10] L. Prandtl. Induced drag of multiplanes. Technical Report TN 182, NACA, March 1924. reproduction of "Der induzierte Widerstand von Mehrdeckern". Technische Ber. 3, pp. 309-315, 1918.

[11] Max Munk. *Isoperimetrische Aufgaben aus der Theorie des Fluges*. Dieterichsche Universitäts-Buchdruckerei, 1919.

[12] R. H. Lange, J. F. Cahill, E. S. Bradley, R. R. Eudaily, C. M. Jenness, and D. G. Macwilkinson. Feasibility Study of the Transonic Biplane Concept for Transport Aircraft Applications. 1974. . NASA CR–132462, Lockheed–Georgia Company.

[13] Aldo Frediani, Vittorio Cipolla, and Emanuele Rizzo. The PrandtlPlane configuration: Overview on possible applications to civil aviation. In Giuseppe Buttazzo and Aldo Frediani, editors, *Variational Analysis and Aerospace Engineering: Mathematical Challenges for Aerospace Design*, volume 66 of *Springer Optimization and Its Applications*, pages 179–210. Springer US, 2012. 10.1007/978-1-4614-2435-2_8.

[14] Community Research and Development Information Service (CORDIS). Prandtlplane ARchitecture for the Sustainable Improvement of Future Airplanes. *PARSIFAL*, 2017. Project ID: 723149.

[15] Giuseppe Persechino, Vincenzo Rosario Baraniello, and Roberto Borsa. Hybrid unmanned inflatable aircraft. International Patent WO 2022/167875 A1, August 2022. Assignee: Centro Italiano Ricerche Aerospaziali (C.I.R.A.).

[16] Yongkao Li, Haoquan Liang, Yan Wang, and Dongxu Liu. Nonlinear response prediction of stratospheric airship envelope differential pressure via multimodal coupling and multiscale decomposition. *Aerospace Science and Technology*, 178:112380, 2026.

[17] Eleonora Riccio, Chiara Giaquinto, Vincenzo Rosario Baraniello, and Domenico Coiro. Preliminary conceptual design of a closed-wing high-altitude pseudo-satellite. *Journal of Aircraft*, 0(0):1–17, 0.

[18] Livermore Software Technology (LST), an Ansys Company, Livermore, CA. *LS-DYNA Keyword User's Manual Volume I*, r13 edition, September 2021. Version R13.0.

[19] Yan Xu, Yilong Yang, He Huang, Gang Chen, Guangxing Li, and Huajian Chen. Multi-objective optimization design of an origami-inspired combined cushion airbag. *Aerospace*, 11(3), 2024.

[20] Harris Edge, Ainsmar Brown, Jason Collins, Rajneesh Singh, Surya Dinvahi, Daphne Pappas, Andres Buhanda, Muthuvel Murugan, Michael Coatney, and Nathan Slegers. Pressurized structures technology for unmanned aerial vehicles (uavs). Technical Report ARL-TR-5436, U.S. Army Research Laboratory, Aberdeen Proving Ground, MD, January 2011. Vehicle Technology Directorate, ARL. Approved for public release; distribution unlimited.